Steering interzeolite conversion with alkali metal cations: lithium maximizes Al proximity in SSZ-13 zeolite genesis

Sven Robijns[1], Julien Devos[1], Thibaut Donckels[1], Rodrigo de Oliveira-Silva[2], Niels De Witte[3], Dimitrios Sakellariou[2], Tom R.C. Van Assche[3] and Michiel Dusselier[1]*

[1] Center for Sustainable Catalysis and Engineering (CSCE), KU Leuven, Celestijnenlaan 200F, B-3001 Leuven, Belgium.

[2] Centre for Membrane separations, Adsorption, Catalysis and Spectroscopy for sustainable solutions (cMACS), KU Leuven, , Celestijnenlaan 200F, B-3001 Leuven, Belgium.

[3] Department of Chemical Engineering, Vrije Universiteit Brussel (VUB), Pleinlaan 2, B-1050 Brussels, Belgium.

ABSTRACT

Zeolites have long been regarded as difficult to modify during synthesis, as their synthesis is governed by kinetic processes. Recent breakthroughs have made it possible to exert a certain degree of control over zeolite properties with more performant materials as a result. Here, we investigate the effects alkali cations have on high-silica FAU-to-CHA interzeolite conversion (IZC) and on the resulting aluminum distributions. In this way, by using Li-cations in conjunction with an organic structure directing agent, the first route to a 'fully paired' (divalent cation capacity, Co^{2+}/Al = 0.48) high-silica SSZ-13 zeolite is demonstrated. Lithium shows great potential in steering IZC synthesis as it speeds up crystallization, and evidence was gathered in favor of a more elaborate mechanism of IZC in which dissolved Al-rich oligomers crash out of solution first and possibly spark nucleation. These findings help in gaining insights into a more general theory on zeolite nucleation in heterogeneous environments such as IZC. Furthermore, the 'fully paired' sample has great potential for ion-exchanged zeolite catalysis or in adsorbents.

1. INTRODUCTION

Due to an increased interest in circularity, mounting resource prices and a shifting focus toward sustainability, industry is striving towards more cost efficient and environmentally benign processes and unit operations, and renewable carbon routes.[1] Small molecules play a key role in this transition as they are often perceived as established platform chemicals (e.g. methane, hydrogen, ethylene and methanol) or are present in flue gasses as the main pollutants (e.g. CO_2, NO_x and SO_x).[2,3] The need to selectively and efficiently separate and process these small molecules into more valuable or less harmful products has never seemed higher. Small pore zeolites are an interesting class of materials in this regard, as their eight-membered ring (8MR) pore mouths (e.g. CHA: 3.72 Å[4]) are in the right size range to allow for easy diffusion of small molecules such as CO_2 (kinetic diameter: 3.3 Å[5]). On top, a lot of 8MR zeolites have large internal cages (e.g. CHA: 9.4 Å X 11.7 Å[6]), that can confine intermediates or active site complexes or provide for adsorption capacity. Aside from this, zeolites, which are already well-established catalysts and adsorbents in processes such as FCC[7,8], NH_3-SCR[9–12], xylene isomerization[13] or ion exchange[14], have lots of clear benefits such as their high thermal stability and capability to act as a support for active transition metals. Yet, when compared to other microporous adsorbents and catalysts[15], modification of the final material product is much more difficult. Zeolite synthesis is a complex and reversible chain of coupled dissolution-precipitation mechanisms that are still not entirely understood by the community[16,17], hence only a few (post-)synthetic handles are known to control the exact outcome. Nonetheless, recent advances in the regulation of aluminum distributions (both siting[18–20] and zoning[21–23]), introduction of mesopores[24–26], and the inclusion of heteroatoms[27,28] (both in the framework and as a counter ion) have shown the ability for such modifications, both

top-down (post-synthetic) and bottom-up (from synthesis), to impact both the selectivity and the activity (uptake in case of adsorption) of these small pore zeolites in a range of processes.

Over the last couple of years, innovative ways of regulating zeolite properties, like charge density mismatch (CDM), microwave- and radical-assisted syntheses, … have been developed.[29] One particular synthesis procedure which has been in the limelight is interzeolite conversion (IZC), also known as interzeolite transformation.[27,30] This is the hydrothermal conversion of one zeolite topology, often an inexpensive FAU, into another, often less commercially available topology.[27] In general, the main benefit of IZC lies in it facilitating the formation of a target zeolite through heterogeneous nucleation, resulting in the rapid formation of relatively small zeolite crystals.[31] Furthermore, whilst the exact mechanism governing the IZC of aluminosilicates still remains elusive to some extent, many theories have been put forward which attempt to explain the inner workings. One of the earliest and most persistent of these theories is the idea that the transformation is facilitated by the transfer of common building units (CBUs) which are present in both the mother and the daughter zeolite.[31] This idea, however, is incomplete as IZC has been observed between two frameworks that don't share any CBUs.[32,33] Recent work by our group shares this train of thought[34,36] and pointed towards the crucial role of aluminum and its interactions with both organic and inorganic structure directing agents (SDA). They showed that in high silica IZC systems, aluminum gets concentrated into a solid phase before crystallization can take place, providing a nucleation point for the process. It was also postulated that the ability of the SDAs in solution to interact with this Al-rich solid phase could predict the course of crystallization, as the addition of Na^+ to an unusually slow IZC towards MFI was able to speed up the process significantly.[36] Interestingly, in 2019, Muraoka *et al.* were the first to pose that IZC could be used to control the arrangement of Al atoms during synthesis. Using ^{29}Si-NMR, they

noticed that a low-Si CHA zeolite synthesized via IZC contained more Q_4(2Al) species than its counterpart synthesized from amorphous starting materials[37], indicating that a clustering of aluminum had taken place during the process.

Control over aluminum distributions has been sought after, as metrics such as the divalent cation capacity (DCC) have been shown to (inversely) correlate to activity and selectivity in reactions such as the dehydration of methanol[38], partial oxidation of methane over Fe-SSZ-13[34], NH_3-SCR[11] and propane cracking,[39] and is defined as the number of divalent cations that can be adsorbed per aluminum (often $\frac{Co^{2+}}{Al}$).[40,41] Dědeček *et al.* were the first to utilize a cobalt exchange to investigate the distribution of aluminum inside a zeolite.[41] Computational studies later showed that in SSZ-13 only paired aluminum sites in 6MRs are energetically favorable sites for Co^{2+}-exchange at mild exchange conditions.[42] In the past, two routes of control over the number of aluminum pairs have been applied. The first route is a kinetic one, such as via IZC. Due to the speed at which crystallization takes place and the densification of aluminum in the solid phase before crystallization, aluminum gets caught in thermodynamically less favored proximate positions.[34] During prolonged synthesis, and dependent on the type of counter ion, this aluminum will then migrate to more isolated positions as dictated by Dempsey's rule[43], resulting in a decrease of DCC over time.[34-36] The second route, based on charge-balancing, is governed more by thermodynamic principles. Altering synthesis parameters such as organic and inorganic SDA[19,45] and counter ions[46] accounts for the majority of literature on modification of Al arrangements via synthesis.

A combined approach deliberately utilizing elements from both the kinetic and the thermodynamic routes is the starting point of this work, although the strict difference between them can be open for discussion and depends on the timescale. Here, this combination of kinetic and thermodynamic

approaches is investigated by looking at: 1) the type and concentration of alkali cations present in the batch and 2) the duration of the synthesis.

2. MATERIALS AND METHODS

Zeolite Synthesis All zeolite syntheses followed a fixed batch recipe using the following composition 1 SiO_2 : $\frac{1}{40}$ AlO_2^-: (0.35-X)$TMAdam^+$: X M^+: 0.35 OH^- : 16.5 H_2O. As a specific example, an SSZ-13 zeolite made with a $\frac{Li^+}{OSDA}$ of 0.2 has a batch composition of : 1 SiO_2 : $\frac{1}{40}$ AlO_2^- : 0.29 $TMAdam^+$: 0.06 M^+: 0.35 OH^- : 16.5 H_2O and is made by the following procedure. Firstly, 0.57 grams of a 10 wt% aqueous LiOH (98% Anhydrous, Acros Organics) solution, 12.51 grams of a 20 wt% aqueous Trimethyladamantylammonium hydroxide (TMAdamOH) solution (OH form, 20 wt% Sachem) and 1.55 grams of de-ionized water (18.2 mΩ) are weighed into a clean 25 ml Teflon liner (Parr instruments, 23 ml acid digestion vessel). A stir bar is added and the mixture is stirred for ~5 minutes at 500 rpm (heat-resistant multiposition stirring plate, 2mag). Next, 2.50 grams of CBV780 (Si/Al=40, H-form, Zeolyst, used as delivered) is stirred into the mixture and left to homogenize for another 5 minutes. The liner is capped and placed inside a steel autoclave (Parr instruments, 23 ml acid digestion vessel). After this, the mixture is placed in a forced convection oven (Heratherm, Thermo Scientific) at 160°C under 600 rpm stirring for a certain time (15 minutes to 8 days). After this period, the autoclave is cooled for 20 minutes under a controlled stream of cool water, after which, the content of the autoclave is transferred into a 50 ml polypropylene (PP) centrifuge tube (50 ml PP tube, Sarstedt) and centrifuged for 20 minutes at 6000 rpm (Thermo Fisher Scientific, SL16). The liquid was decanted and kept for pH measurements, whilst the solid was washed. For the washing of the solid phase, ~35 ml of de-ionized water was added to the centrifuge tube after which it is shaken in order to bring all solids

into suspension. Next, it was centrifuged for 20 minutes at 6000 rpm and all liquids were decanted and discarded. This procedure is repeated at least 3 times until the pH of the mixture drops below 9. Finally, the solids are washed one last time with 20 ml of acetone and kept in an oven at 60°C overnight for drying. Solid yields were determined by weighing the solid fraction after this drying step and applying a correction factor based on the weight loss obtained by TGA. For the temporal study of the Li system, each datapoint represents a separate batch reaction with a $\frac{Li^+}{OSDA}$ of 0.2 or 0.5, and an oven time (at 160°C) between 15 min and 8 days. Due to the low reaction times, and some of the autoclaves not reaching thermal equilibrium, extra attention was put into timely extraction from the synthesis oven and uniform cooling under a controlled stream of cool water for these syntheses.

Calcination The dried zeolites are calcined to remove the SDA and free up the pores for further analysis. This is achieved by heating the powder in a muffle oven to 580°C with a ramp of 1°C/min under air (LV9/11, Nabertherm). After, these zeolites are transferred into a closed container to mitigate the uptake of water from the atmosphere. Weights before and after calcination are noted down.

Ion exchange For the determination of the DCC an ion exchange was conducted. Calcined zeolites were suspended three times in 150ml of a 0.5 M solution of NaCl (>99%, VWR) under 600 rpm stirring for respectively 16, 8 and 16 hours. This procedure is then repeated with 150 ml of a 0.05 M solution of $Co(NO_3)_2$ (>99%, Acros Organics). After this, the product is washed 3 times with de-ionized water and dried at 60°C overnight.

X-ray powder diffraction. The structure and crystallinity of the zeolites were confirmed by X-ray powder diffraction (PXRD) on a high-throughput STOE STADI P Combi diffractometer in

transmission mode with focusing Ge(111) monochromatic X-ray inlet beams (λ = 1.5406 Å, Cu Kα source). For each sample, a beam time of 10 minutes is used.

Nitrogen physisorption. Porosity is measured by nitrogen physisorption (Tristar II 3020, micromeritics) at -196°C on calcined and dried samples (≥6 h at 300°C). The relative nitrogen pressure is varied between 0.01 and 0.99 (p/p_0). The t-plot method (Harkins and Jura) on the adsorption branch is used to determine micropore volumes.

Elemental analysis. Before ICP-AES, the samples were dissolved using HF. This was done by adding 1 ml of HF (40% in water, Chem-Lab Analytic) and 0.5 ml of aqua regia (3:1 volumetric mixture of concentrated HCl (37%, for analysis, Acros Organics) and concentrated HNO_3 (65%, for analysis, Acros Organics)) to 50 mg of the sample inside of a 100 ml PP bottle. *Caution: Working with HF is very dangerous and should only be performed by trained personnel under a fume hood using sufficient personal protection.* After 3 hours, the mixture was neutralized using 15 ml of a 30 g/l solution of boric acid (>99%, Fisher Scientific), after which the volume is increased to 100 ml using de-ionized water. Finally a further dilution by a factor of 26 is done by the addition of 0.42 M of HNO_3. The elemental analysis was performed using an inductively coupled plasma-atomic emission spectrometer (ICP-AES, Perkin Elmer Optima 3300 DV) with signals for Co, Al, Si and Li at 308.2, 238.2, 251.6 and 670.8 nm respectively.

Thermogravimetric analysis. TGA for as-synthesized SSZ-13 was performed on a TA Instruments TGA Q500 under 90 ml/min of O_2. The heating rate was set at 10°C/min up until 800°C.

TEM. Transmission electron microscopy (TEM) of the samples was performed with an aberration-corrected JEOL ARM200F Microscope operating at an acceleration voltage of 200 kV

and equipped with a cold FEG. Dark-field imaging was performed in Scanning TEM (STEM) mode with an annular dark-field (ADF) detector. The samples were prepared via drop-casting a sonicated particle suspension on a holey carbon-coated TEM grid (Cu, 400 mesh, Agar Scientific).

Energy Dispersive X-ray spectroscopy (EDX) EDX analysis of Si, O, and Al in the samples was carried out utilizing a Centurio EDX detector with a solid angle of 0.98 steradians from a 100 mm^2 detection area.

^{27}Al Solid-State NMR. The solid-state NMR experiments were performed with Bruker Avance I spectrometer using a 4mm Chemagnetics solids probe at a 500MHz Oxford wide-bore superconducting magnet. The powdered samples were introduced into the 4mm rotors to perform the MAS (magic-angle spinning) experiments. Single-pulse (onepulse.av) experiments were performed at 15kHz of MAS, with pulse width equal to 3μs, and repetition delay of 4.5s. The spectral window was 100kHz and the number of acquisition points was 2048. Before being Fourier transformed, the FIDs were zero-filled to 16k points and apodized with 20Hz of linear broadening. The chemical shift was referenced to the reference Al_2O_3 solution.

3. RESULTS

The main focus here is the effect that different alkali cations have on the conversion of a high silica USY zeolite (Si/Al=40) to SSZ-13. Mainly, the Al distributions and elemental composition are probed to get a better insight into the mechanisms governing IZC and to expand control over Al arrangement. It is important to mention that the investigations into the effects of inorganic cations have already been undertaken several times, by multiple research groups[11,19,45,47], yet IZC systems didn't belong to the scope of their work. The recipes used in this work are slightly modified in-house CHA recipes (see Methods)[34]. Finally, a distinction needs to be made between the terms proximate and paired alumina, which are sometimes used interchangeably. Proximate alumina, used here, describes all Al sites which can exchange hydrated cobalt cations. However, DFT suggests that in the case of SSZ-13 the majority of proximate Al exchanged by cobalt are actually paired Al (Al-O(-Si-O)$_{1\text{ or }2}$-Al) in a 6MR, which can stabilize both hydrated and dehydrated Co^{2+}.[42]

The effect of alkali cations on the synthesis

When comparing the Si/Al ratio as a result of crystallization after 6h using different cation concentrations (Figure 1A), two different regions of interest can be observed: a region with low ($\frac{M^+}{OSDA}$<0.5), and high (0.5<$\frac{M^+}{OSDA}$) alkali cation concentrations.

Firstly, in the region of low inorganic cation concentration ($\frac{M^+}{OSDA}$ <0.5), an interesting trend can be observed: as the alkali concentrations increase, the Si/Al ratio appears to evolve in the following order: $K^+ > Na^+ > Li^+$. At first, this seems counter-intuitive as KOH is the strongest base of the three, but zeolite dissolution has been shown to depend on the total hydroxide concentration and not on the type of alkali cation.[48] This Si/Al effect thus likely is caused by other factors such as charge density or cation size. Early research by Nagy *et al*. indicated that in systems with a mix of alkali and OSDA cations, the one with the highest charge density, often the alkali cation, will preferentially interact with dissolved alumina species[49]. It is also known that larger cations, like K^+, are capable of stabilizing bigger dissolved silicate oligomers in solution than smaller cations like Li^+.[50–52] Subsequently when crystal growth commences, these alkali cations will incorporate aluminosilicate oligomers with a varying amount of Si and Al into the framework, resulting in a Si/Al ratio dependent on the chosen alkali cation.[53]

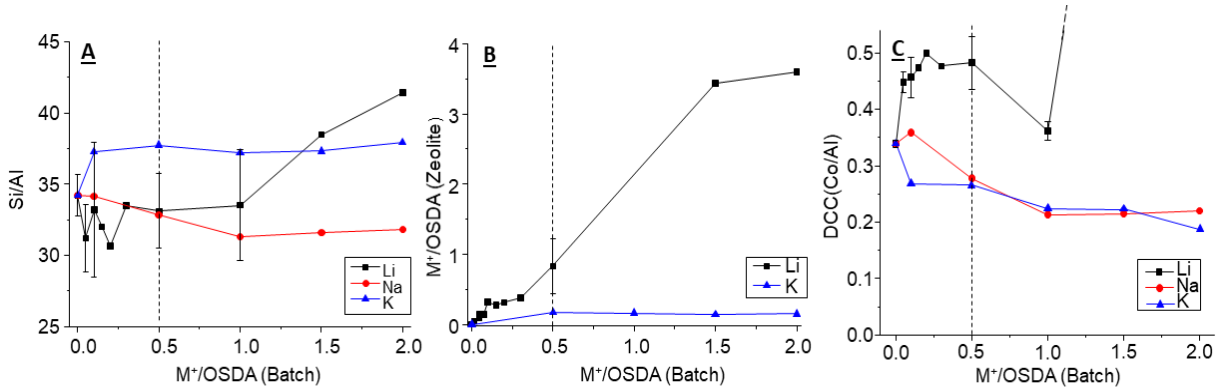

Figure 1: (A) The Si/Al ratio and **(B)** the M^+ content of the synthesised zeolites; and **(C)** DCC of an IZC system under different concentrations of Li^+, Na^+ and K^+ hydroxides. All syntheses were conducted for 6h at a temperature of 160°C. The batch composition was as follows: 1 SiO_2 : $\frac{1}{40}$ AlO_2^- : (0.35-X) $TMAdam^+$: X M^+: 0.35 OH^+ : 16.5 H_2O. Error bars indicated on the plots represent the margin of error obtained from multiple repetitions of synthesis, most of the variance is due to samples being measured in different ICP-sessions. The number of samples represented in each error bar in **(A)**, from left to right is: 3, 3, 2, 6 and 3. The extended DCC plot for the Li sample can be found in figure S1.

At high alkali concentrations (0.5<$\frac{M^+}{OSDA}$) for the K^+ system, and at even higher $\frac{M^+}{OSDA}$ exceeding 1 for the Na^+ system, changes in Si/Al ratio seem to be much less pronounced in response to changes in alkali concentrations in comparison to at low concentrations, suggesting that excess alkali

cations are not incorporated into the daughter zeolite. On the other hand, the Li^+ system appears to experience a rapid increase in Si/Al at $\frac{Li^+}{OSDA}$ ratios above 1. A partial explanation for this could be the amount of both K^+ and Li^+ which gets taken up by the zeolite during synthesis (Figure 1B). For the potassium system, the zeolite only shows an increased uptake of K^+ at low concentrations after which no additional K^+ is incorporated into the zeolite anymore due to an increase in the batch content. This seems to be in contradiction to the observations made by Di Iorio *et al.,* who observed that high concentrations of K^+ in the synthesis liquor would result in the displacement of OSDA from the zeolite cages and thus an increased K^+ content in the final product.[19] These differences are explained by the lower Al content of the IZC system, reducing the amount of available sites for K^+, and the much lower batch concentration of K^+, as Di Iorio *et al.* studied systems with a $\frac{K^+}{OSDA}$ ratio as high as 20 and products with Si/Al ratios as low as 6.8.[19]

The Li^+ system shows different behavior though, showing a good positive correlation between the concentration of Li^+ in the batch and the daughter zeolite. These rising concentrations of Li^+ inside of the daughter zeolite indicate a tipping point in which the Li^+ (and OSDA) content of the daughter zeolite climbs past the Al content of the zeolite, necessitating the presence of defect sites for charge balance. The high charge density of Li^+ is ideal for stabilizing these defects in more silicious environments.[49,54] At very high concentrations, the Li^+ system experiences a rapid increase in Si/Al ratio, with a concomitant decrease in pore volume (Figure 2 (right) & Table S1). XRD spectra (Figure 2 (left)) confirm the presence of a layered lithium silicate $Li_2Si_2O_5$ in the synthesis output, increasing the Si content of the bulk output, which is not a pure zeolite anymore. This material consists of single layers of silica tetrahedra, each of which is connected to three other silica tetrahedra.[55] The fourth corner of the tetrahedron is occupied by a $Si\text{-}O^-\ Li^+$ species, all of which

are pointed towards the interplanar void (Figure S2). This material has no (micro)porosity, hence the reduction in uptake of N_2.

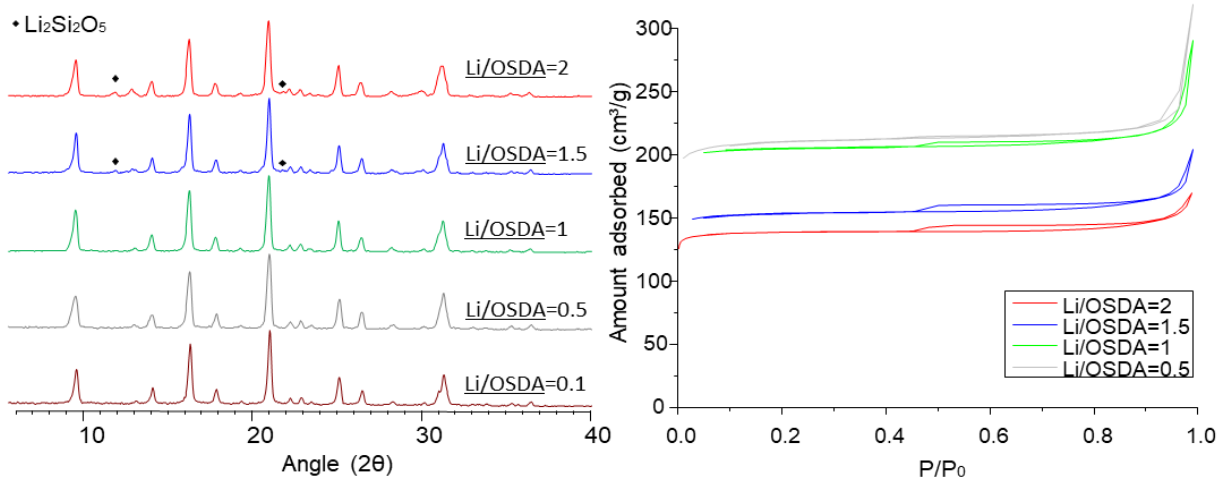

Figure 2: (Left**)** XRD spectra and (right**)** N_2 physisorption of IZC syntheses using different Li/OSDA ratios. The peaks appearing at 12° and 22° in the XRD spectrum are characteristic of $Li_2Si_2O_5$. Micropore volumes are listed in Table S1 and show lower Li/OSDA ratios didn't result in a drop in pore volume compared to a reference sample without Li.

Figure 1C displays the trends followed by the DCC as different concentrations of alkali cations are added to the synthesis mixture. At a $\frac{M^+}{OSDA}$ ratio of 0, the DCC ratio ($\frac{Co}{Al}$) is equal to 0.34, which indicates 68% of the Al are proximate alumina. This is similar to the results reported by Devos *et al*. for a similar recipe and is, up to now, the highest obtained value in high silica SSZ-13.[34] At increasing alkali concentrations, two different behaviors can be observed. Firstly, Na^+ and K^+ systems show a decrease in DCC at higher alkali concentrations. Especially for the K^+ system this is an unexpected result as factors such as Si/Al ratio, crystallinity and K^+ and OSDA concentration in the daughter zeolite all remain constant (Figures 1A, 1B, and S3) under increasing alkali ratios. This result displays that the DCC is not only dependent on the final concentration of alkali cations in the daughter zeolite, but also gets impacted by the presence of alkali in different (kinetic) stages of zeolite synthesis such as dissolution, induction or crystal growth phases.

Secondly, the most interesting of the three curves displayed in figure 1C consists of a system experiencing different Li^+ concentrations. A clear influence can already be observed when looking

at the addition of low concentrations of Li^+ ($\frac{Li^+}{OSDA}$<0.5), which are in the same range as the total Al concentration inside of the synthesis liquor: an immediate jump in DCC to higher values is observed when adding Li^+. It can be seen that the addition of the lowest concentrations of Li^+ has the biggest effect on the DCC as a sudden increase is observed from 0.34 to 0.44 between a $\frac{Li^+}{OSDA}$ ratio of 0 and 0.05. The further increase in lithium to a value of 0.2 results in a modest increase from a DCC of 0.44 to 0.48. This would indicate that in an ideal case nearly 100% (96%) of the Al would be in a proximate state. One indication of this being the case, is the observation that at $\frac{Li^+}{OSDA}$ ratios between 0.2 to 0.5 the DCC reaches a plateau at 0.48 whilst Li^+ keeps being accumulated in the daughter zeolite (Figure 1B). This suggests that the Al concentration (and configuration) is indeed the limiting factor in the uptake of Co^{2+} (and thus establishing DCC measurements here to be correct) as stabilization of Co^{2+} by siliceous defects, opposed to proximate Al, would likely result in a DCC surpassing the theoretical maximum in pure phase zeolites. Additional proof excluding the presence of Li^+ during the Co-exchange to be the culprit

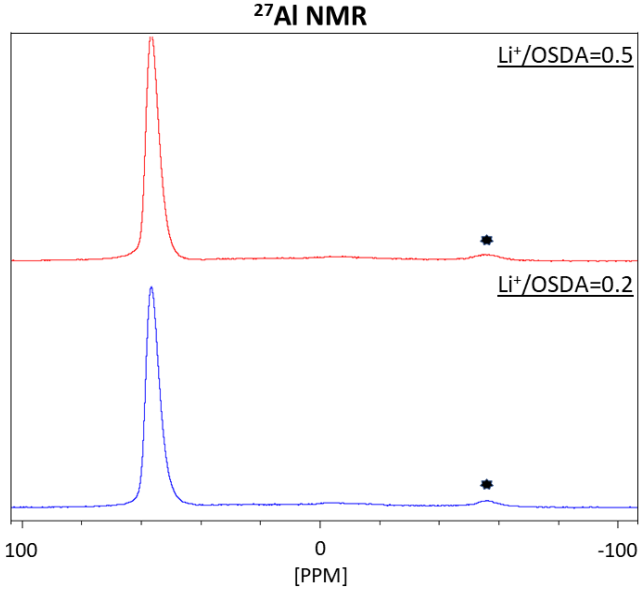

Figure 3: MAS ^{27}Al-NMR of 2 calcined zeolites synthesized using different Li/OSDA ratios. The star indicates a spinning sideband. The signal at 58 ppm indicates all Al is in tetrahedral coordination.

for the high Co^{2+} uptake, based on charge balance, can be found in the supplementary information (Figure S5). Furthermore, ^{27}Al solid-state NMR spectra indicated that both at $\frac{Li^+}{OSDA}$ ratios of 0.2 and 0.5, most of the alumina is in a tetrahedrally coordinated form before and after calcination (Figure 3). The role of Li^+ in making the formation of proximate Al sites more thermodynamically favorable had already been discovered by Lv *et al.*[11] yet by utilizing amorphous starting sources they were not able to fully capitalize on this effect, reaching DCC values below 0.3.

Finally, at the highest $\frac{Li^+}{OSDA}$ ratios the DCC increases significantly to values above 0.5, which means proximate Al sites can't be responsible for this increase. Yet, above 0.5, the presence of the lithium silicates formed at these conditions is believed to be causing this effect, as such silicates likely have some affinity towards the adsorption of cobalt due to their layered structure and dangling Si-O^- bonds in the interplanar space (See figure S2). Additionally, similar materials, namely calcium silicate hydrates, are known to be capable of adsorbing certain amounts of cobalt.[56] The next paragraph attempts to elucidate the critical role Li^+ cations play in Al-pair genesis.

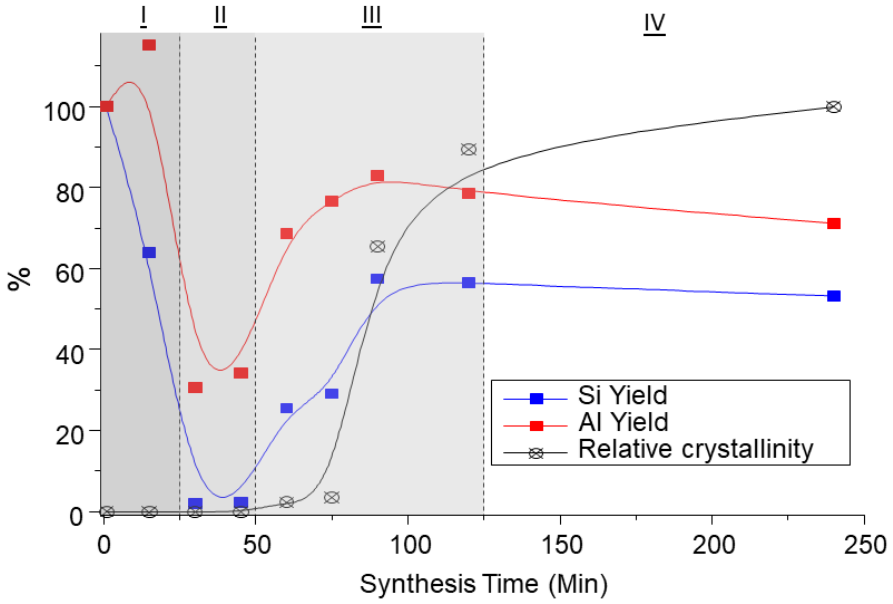

Figure 4: Relative crystallinity and Si and Al yield of a synthesis system with a Li/OSDA of 0.2 as a function of synthesis time. A bezier-spline fit of the data was used as a guide to the eye.

Further elucidation of the mechanisms governing IZC with Li

To get a better understanding of the mechanisms which govern IZC and the interesting Li effects, a closer look was taken at the full crystallization course of two FAU-to-CHA systems with a $\frac{Li}{OSDA}$ ratio of 0.2 (vide infra) and 0.5 (Figures S6 & S7).

Figure 4 shows the course of the Si and Al yields and the relative crystallinity during the synthesis procedure. Note the presence of the different stages of high silica IZC (I-IV) as described by Devos *et al*.[34] First, a dissolution stage (I) is observed where silica incongruently dissolves leaving an alumina rich solid behind. After 20 to 30 minutes, an induction phase (II) occurs in which not much change is noted. Next, after 60 minutes total time, crystal growth commences and a significant increase in both yield (Figure S8) and crystallinity is observed (III). Both of these variables follow a typical sigmoidal (S-)curve associated with crystal growth.[16] The pH in the liquid phase also experiences a strong increase in this timeframe (Figure S9) signaling that the condensation of oligomers is occurring. Interesting to note is the pace at which these processes take place. Previously reported SSZ-13 syntheses using only organics took at least 150 minutes to obtain high crystallinity[34], whilst here relative crystallinity already reaches ~70% after 90 minutes, being fully completed after 105 minutes. This is a key example of Li^+ (and Na^+) being able to speed up the crystallization of a zeolite due to them being water structure forming cations in opposition to K^+ being a water structure breaking cation.[50,57] This indicates that Li^+ can strongly coordinate with water and (alumino)silicate oligomers which leads to a faster formation of the zeolite. Interesting to note is that in the art, LiOH causes the dissolution of silicates to slow down with respect to a system with lower charge density, such as KOH, as its high charge density makes

it difficult for Li^+ to dissociate from its OH^-.[51] No such effect was observed in the Li^+ containing IZC system.

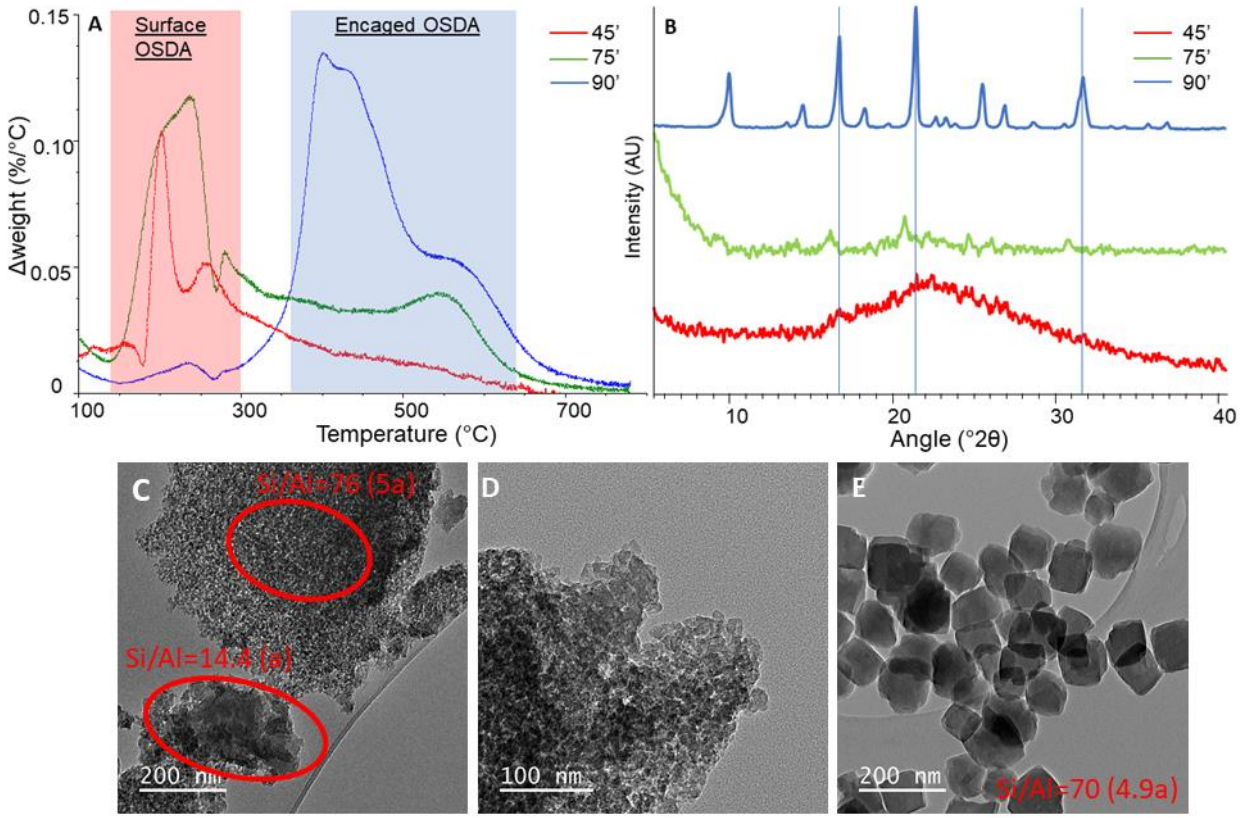

Figure 5: (**A**) DTG profiles of the Li^+/OSDA=0.2 after 45,75 and 90 minutes. Two regions are observed in the profile for the burn off of adsorbed 'surface' OSDA and encaged OSDA. (**B**) X-ray diffractograms of the same samples with some characteristic peaks indicated. TEM images of the synthesis at 75 minutes (**C-D**) and after synthesis has completed (**E**) at 120 minutes. The Si/Al values in red are measured by EDX, yet no external standard was used. Obtained Si/Al values can thus only be used in comparison relative to each other and are also displayed in function of a common factor a.

Interestingly, the Si yield in figure 4 increased with a delay compared to the Al yield, and assuming supersaturation is high enough for the majority of dissolved species to be oligomers, this indicates that Al-rich oligomers are the first ones to come out of solution and be incorporated into the zeolite. This first cohort of oligomers is then followed by a series of more siliceous oligomers until the crystallization has come to an end. Notable is that even after crystallization finishes based on the S-curve, there is still some Al which remains in solution as the Al yield only reaches a maximum of approximately 80%. To obtain a better understanding of this region of interest between 60 and 90 minutes, more in-depth characterization was performed (Figure 5). Figure 5A displays

differential thermogravimetric analysis (DTG) profiles of samples taken before (45 min), during (75min) and after (90min) crystallization took place. Two key areas in these profiles can be observed: a region between 150-300°C which represents non-encaged OSDA which is still able to evaporate from the solid phase and a region which shows significant weight loss at higher temperatures than 300°C. Changes in this higher temperature region are only visible in (partially) crystalline samples and thus represent OSDA which is encaged inside the pores and cages inside of the zeolite. Next, as the synthesis progresses from the induction phase to the crystallization phase, organics start to get incorporated into the zeolite framework and together with the first crystallinity in XRD (Figure 5B), an increase in the burn-off at higher temperatures is noticed. Finally, when crystallization is finished, most of the burn-off of OSDA occurs in this region. It is thus likely that crystallization is occurring at the surface of the Al-rich solid phase as no encaged OSDA is observed at 45 minutes. Further investigation of the XRD results in figure 4B lead to some compelling observations. Firstly, the first crystalline peaks are formed between 45 and 75 minutes indicating the presence of the first crystalline material before most of the solids have precipitated from solution. Secondly, and perhaps more significant, the reflections at 75 minutes show a shift to lower angles in comparison to the fully crystalline sample at 90 minutes. Such a shift indicates an expansion in lattice parameters, most often associated with the presence of a high quantity of Al inside of the framework as Al-O bonds are slightly longer than Si-O bonds.[58–60] This gives the impression that the first nuclei to form are more aluminous than the final product.

TEM pictures taken of samples that experienced 75 minutes (Figure 5C-D) of hydrothermal synthesis showed an agglomeration of smaller particles together with the presence of one bigger and texturally different particle. These small particles are structurally similar to the worm-like particles observed in the work of Kumar *et al.* and together with the irregular morphology of the

daughter zeolite hint at a non-classical mechanism of growth lying at the basis of IZC.[61] Crystallization by particle attachment is common in systems with high super saturation, such as IZC, and generally leads to irregular crystals and a fast synthesis. This is the case as can be observed in figure 4E. The size and the shape of these crystals are similar to the ones observed in existing literature utilizing similar batch compositions.[34] Finally, EDX was utilized to map the elemental gradients of both Si and Al inside of the crystals. (Figures S10 & S11) No internal standard was used when determining Si/Al ratios with EDX, thus the values obtained can only be compared relative to each other. Whilst after 120 minutes, Si/Al ratios were quite uniform across different particles and no Al zoning is detected within a single particle, some inhomogeneities are detected at 75 minutes. The texturally different particle which was observed, appeared to have a lower Si/Al ratio (Si/Al=a), the worm-like particles in contrast appeared to have a similar Si/Al ratio (Si/Al=~5*a) to the daughter zeolite (Si/Al=4.9*a, figure 5E, 120 minutes), within experimental error. The big alumina rich particle appears to be a remnant of the Al-rich solid phase during the induction stage of IZC.[34] In TEM (Figure 5D, 75 minutes), no crystalline domains have been observed to be present already. Yet, the appearance of crystalline peaks in XRD indicates a presence of crystalline (Al-rich) particles which cannot be observed in the TEM. A possible explanation for this could be that the first nuclei are rather small and well dispersed throughout the synthesis medium, making them difficult to detect. However, once a viable CHA nucleus has formed, the crystal growth can proceed at great speed through rapid attachment of the worm-like particles.

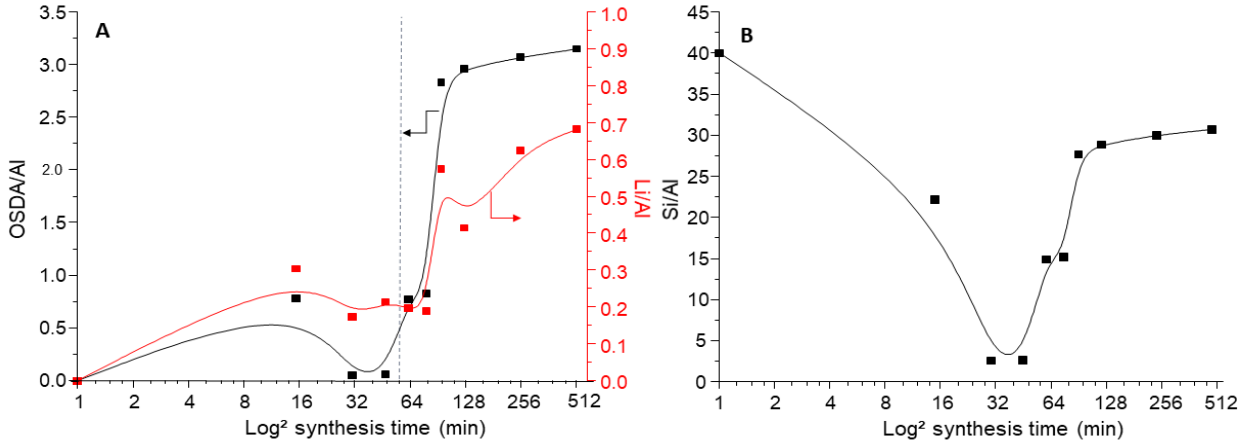

Figure 6: (**A**) The $\frac{OSDA}{Al}$ and $\frac{Li+}{Al}$ ratios of the solid phase of a system using a batch $\frac{Li}{OSDA}$ ratio of 0.2 as a function of the synthesis time. The $\frac{Si}{Al}$ ratio is shown in (**B**) as an indication that the Al content in (**A**) is relative. OSDA is quantified using TGA, Al, Li en Si using ICP. The faint line in (**A**) represents the boundary between stage II and III of IZC. A bezier-spline fit of the data was used as a guide to the eye.

Detection of the alkali cation content during synthesis, similar to the work of Chawla *et al.*[62] would give a revealing look into the systems course of actions, however lithium is too light to be detected by EDX. This means only bulk detection methods such as ICP-AES are capable of following the action of lithium during the synthesis, at the cost of resolution on different phases inside of the synthesis liquor. This bulk analysis of the zeolite still holds valuable information, especially when compared to the course of the second cation in solution, namely the OSDA. (Figure 6A) The data is represented as a $\frac{cation}{Al}$ ratio, which is coupled to the Si/Al ratio. The Si/Al ratio of the solid phase, obtained from the Si and Al yields in figure 3, is thus depicted in figure 6B for comparison. During the course of the synthesis, both the Li^+ and the OSDA show similar behavior. Firstly, some of the OSDA is exchanged onto the dissolving zeolite, after which they are (mostly) expelled as the zeolite breaks down further. Compared to the OSDA, Li^+ has a slightly higher tendency to stay coordinated to the Al-rich solid phase. After this there are some slight differences between both cations and their behavior during the crystallization phase. During the initial increase in Al yield and Si yield (Figure 4) from 45-75 minutes, the Li/Al ratio stays similar

to the one of the Al-rich solid phase, whilst the OSDA/Al ratio increases significantly. During the second stage of growth from 75-90 minutes, both the Li/Al and OSDA/Al experience a second significant increase.

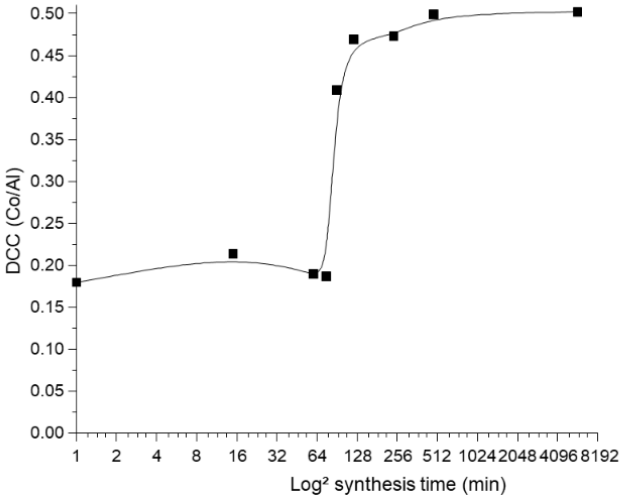

Figure 7: The divalent cation capacity of the solid phase of a system using a batch $\frac{Li}{OSDA}$ ratio of 0.2 as a function of the synthesis time. Note that below 75 minutes, this number has little to no value as the samples are not purely zeolitic. A bezier-spline fit of the data was used as a guide to the eye.

Finally, the DCC of the system was monitored as the synthesis prolonged. The results of this investigation are shown in figure 7. The measurement of DCC during amorphous stages shows the ability of amorphous fractions to take up significant amounts of Co^{2+} during the exchange, in line with our earlier work.[36] Caution should always be maintained during DCC analysis of not fully crystalline samples, as factors other than proximate Al can play a substantial role. Interesting to note is the sudden increase in DCC between 75 and 90 minutes. This coincides with the final stages of crystallization, as the relative crystallinity jumps from 3% to 65% in this timeframe (Figure 4), and indicates the formation of a continuous pore system that is fully open after calcination. Finally, after 120 minutes the DCC remains at a stable plateau for a prolonged time (end of stage III, Figure 4). Previous studies showed the DCC of CHA to decrease during longer synthesis times in IZC unless Na^+ was added to the synthesis.[36] These results indicate Li^+ has a similar effect and provides

thermodynamically stable sites for Al pairs with prolonged oven time (hydrothermal times) up to 12 days (Figure S7).

4. DISCUSSION

To combine the benefits of the thermodynamic and the kinetic routes to control Al distributions, alkali metals were added to an IZC synthesis with great effect. The used alkali cations can be subdivided into two categories. The first one contains the water structure breaking cations such as K^+, which aren't able to strongly coordinate with dissolved aluminosilicate oligomers, causing them to slow down crystallization relative to other alkali cations and incorporate more silica.[50,57,63] On top, in the case of CHA, K^+ doesn't occupy the double six-membered ring (D6R) due to its size and will thus not lead to the thermodynamic preference to form 6MR paired Al sites.[19] The second group is that of Na^+ and Li^+, both are water structure forming cations which at low concentrations benefit the formation and retention of 6MR paired Al sites,[19] partly due to their strong and preferential interaction with Al-containing oligomers.[49] One interesting observation, which is often regarded as a consequence of the course of actions a zeolite undergoes during IZC, is the high DCC obtained during an IZC syntheses. Unlike conventional syntheses, using amorphous precursors and alkali cations (cfr. Di Iorio *et al*.), (metastable) proximate Al sites are created during alkali-free IZC, while fully isolated Al would be expected in line with Dempsey's rule of charge separation[43]. Furthermore the Al-distributions shifts towards isolated sites with prolonged hydrothermal exposure occurring after crystal assembly.[34] How are these proximate sites created (i.e. high DCC in alkali free IZC), when Dempsey's rule clearly states them to be metastable? The densification of Al into an Al-rich phase (Figure 4), the initial formation of more Al-rich crystalline material (Figure 5B), literature on both the role of Al-rich oligomers (Al-O-Si-O-Al) in these systems,[32] and the crystallization mechanism of CHA as observed by Raman

spectroscopy[64], hint to an evolution of two alumina being 'carried into' the new crystal from or in the same aluminosilicate oligomer. We hypothesize that the addition of Li^+ together with OSDA into the synthesis mixture strongly directs the incorporation of these linked alumina in proximate framework positions in which they are capable of exchanging hydrated Co^{2+} (Figure 7). Other cations such as K^+ or Na^+ do not show this effect to such an extent, either because they are not preferentially sited in the D6R (K^+)[19] or are not charge-dense enough to direct all of the Al to be in a proximate position where they can exchange Co^{2+}, as can be seen to be the case for Na^+ in figure 1C. In essence, a synthesis route via IZC is thus capable of delivering the right building blocks for the creation of proximate alumina sites in the presence of Li^+ and the OSDA. Whilst, later on after crystallization, these proximate Al sites can be thermodynamically stabilized by the charges of both the Li^+ and the OSDA. Furthermore, Li^+ is not only an interesting cation to add for reaching the highest DCC, but also because it speeds up the crystallization. This acceleration of stage III causes the Li^+ system to appear more sequential than an alkali-free system: in such sequential fashion, normal overlap to some degree (as in an alkali-free system) e.g. of the precipitation of Si and Al rich oligomers and the crystallization of these nuclei into a crystalline solid, is thus avoided. This allowed for a depiction of the course of crystallization of an IZC system in greater detail than before.

The four stages of IZC will now be discussed, with an emphasis on new aspects (= via referrals to earlier figures) and a cartoon summary in Figure 8. Firstly, incongruent dissolution of the FAU will take place, as silica-rich oligomers will dissolve first. During stage I (dissolution) a partial exchange of the dissolving mother zeolite with both OSDA and alkali cations will take place, presumably aiding in the further dissolution of the FAU[65] and providing some shielding to the dissolving oligomers. Stage II (induction) is characterized by an Al-rich solid phase, which has

expelled all of the OSDA exchanged on the dissolving mother zeolite. Alkali cations on the other hand will likely be well mixed inside of the Al-rich solid phase as was shown in figure 6A. Stage III (crystallization) starts with aluminosilicate oligomers coming out of solution first followed by more silicious ones, as indicated by the early increase of the Al yield (Figure 4) together with XRD results (Figure 5B). Whilst this is the first direct observation of this phenomenon during IZC, it has already been hypothesized in the work of our group (Devos *et al.*)[34] and observed in synthesis from amorphous sources,[35] indicating the nucleation of CHA to take place in a more aluminous context. Al-rich oligomers are rapidly insolubilized and form worm-like particles from which further crystallization can take place, as can be seen from TEM (Figure 4C-E). The roles both the OSDA and Li^+ played in this assembly stage (III) were further elucidated, delivering some key insights in the process. Firstly, in line with literature,[49] it was shown in figure 1 that higher charge density cations show a greater affinity towards interacting with Al during synthesis, giving an explanation to their ability to steer Al distributions. Secondly, the Li/Al ratio (Figure 6A) kept a steady plateau during stage II and early in stage III (30-75 min), despite the Al yield experiencing a rapid increase. This is probably an indication that the interaction of Li^+ with aluminosilicate oligomers in solution is similar to the interaction with the oligomers in the Al-rich solid phase, hinting at them being akin in chemical nature, and thus facilitating the transfer of Li associated with Al into the zeolite in a similar fashion. Thirdly, a large fraction of the cations (both Li^+ and $TmAdam^+$) are incorporated after all of the aluminum has condensed (later in stage III, 75-120 min), resulting in building more silicious fractions. In this case, the OSDA plays the role of template, whilst the Li^+ is responsible for the stabilization of defects.[54] Taken together, it appears that during stage III Al-rich nuclei and worm-like particles are formed first at the surface (Figure 5A) of the Al-rich fraction left after stage II, which probably already contain proximate Al sites.

Lithium is mainly incorporated as a counter ion for aluminum and, according to the DTG results in figure 4A most of the OSDA, at this point, is still not incorporated into rigid pore structures but loosely associated in proto-zeolite type structures. Later in stage III, silica rich oligomers will also precipitate from solution, as the 'pre-aged' worm-like particles rapidly crystallize into the CHA structure. Both OSDA, as a template, and Li^+, probably to stabilize defects as the charge balance ((OSDA+Li)/Al) surpasses 1, will be consumed by the solid phase and incorporated into the zeolite. Stage IV (maturation) doesn't show large changes anymore as the DCC and Si/Al remain stable for a long period of time. The synthesis can be considered finished after only 120 minutes.

In conclusion, IZC has a high potential for delivering high DCC zeolites (fully paired (~proximate), high silica) due to the densification of aluminum and the rapid crystallization kinetics, whilst alkali cations are capable of exploiting this potential by preferentially interacting with Al and thermodynamically stabilizing proximate Al sites.

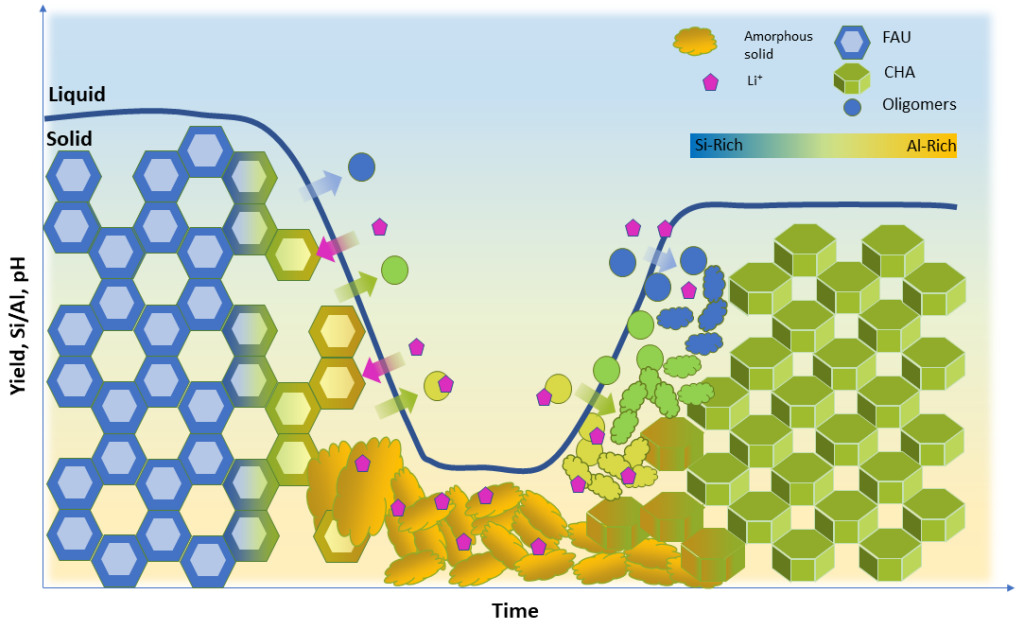

Figure 8: A proposed schematic for the course of a high silica IZC with Li.

5. CONCLUSION

In this work, the roles of alkali metals, mainly Li^+, Na^+ and K^+, during interzeolite conversion (IZC) of FAU-to-CHA has been subjugated to an in-depth study on the effect of concentration, using different analysis techniques such as ICP-AES, XRD and N_2 physisorption among others. An SSZ-13 sample in which approximately 96% of the Al appears in a proximate configuration (Co/Al=0.48) was obtained when the Li/OSDA ratio of the synthesis mixture was between 0.2 and 0.5. The most promising synthesis for DCC was subjected to a temporal study, which led to further insights into the mechanisms governing IZC and by extension zeolite synthesis. Not only was the potential for Li^+ to fully increase the DCC of an SSZ-13 zeolite shown, unlike Na^+ or K^+, but other key observations were also made, including: the acceleration of SSZ-13 crystallization in the presence of Li^+, the formation of Li-silicates at high batch Li concentrations and the crystallization of SSZ-13 taking place from Al-rich CHA nuclei.

The role of Li^+ during the genesis of proximate Al sites was observed to be twofold: both thermodynamic and kinetic effects played their part (although semantics of the distinction between both depends on the timescale). Thermodynamically, this is thought to happen through the electronic stabilization of the paired Al sites inside of the 6MR unit of CHA; while kinetically, via speeding up the crystallization stage, resulting in a metastable outcome with more inhomogeneous local arrangement of Al in the daughter zeolite. Bigger cations, such as K^+ didn't show this effect, mainly due to their bigger size and subsequently lower charge density and different siting in the framework with respect to smaller cations. Further, a mechanism of growth similar to the non-classical growth by particle attachment was also deemed to be likely during IZC. This model is proficient in explaining the high DCC obtained during IZC syntheses: the densification of Al in an Al-rich solid phase from which rapid nucleation and crystal growth takes place, has a high potential

for creating grouped Al, whilst certain alkali cations are subsequently capable of thermodynamically (de)stabilizing the proximate Al clusters during and after crystallization

In general, the results discussed here could lead to the synthesis of better catalysts for redox and acid catalysis, as control over acid site distributions is highly sought after in these fields and fully paired samples are hard to come by. The synthesis of 'fully paired' SSZ-13 zeolite thus opens the door for more in-depth research into the effect proximate alumina sites exert on catalysis and adsorption. Additionally, the investigated system with Li is one of the fastest observed (<2h to fully crystalline products), using conventional batch methods. Conclusions drawn from this research are in all likelihood transferable to other synthesis (IZC) systems where nucleation is favored in aluminous conditions.

ASSOCIATED CONTENT

Additional figures can be found in Supporting Information (SI) (.docx).

AUTHOR INFORMATION

Corresponding Author

*Corresponding author: michiel.dusselier@kuleuven.be

Author Contributions

The manuscript was written through contributions of all authors. All authors have given approval to the final version of the manuscript.

Notes

The authors declare no competing financial interests.

ACKNOWLEDGMENT

S.R., N.D.W., T.V.A. and M.D. thank the Research Foundation—Flanders (FWO Vlaanderen) for funding (Grant G085220N). M.D. acknowledges funding from a Starting Grant from the European Research Council (ERC-2020-STG 948449, Z-EURECA). J.D. acknowledges KU Leuven for a PDM grant (3E210695) and Research Foundation—Flanders (FWO Vlaanderen) for funding (Grant 12E4623N). D.S. and R.O.-S. are grateful for the KU Leuven Starting Grant to D.S. and by the Research Foundation—Flanders (FWO Vlaanderen) under Grant PorMedNMR (G0D5419N) to D.S. SACHEM is explicitly thanked for providing the organic structure directing agent (TmAdamOH). The authors would also like to thank Prof. Jin Won Seo for her support for TEM imaging/troubleshooting and the Hercules Fund (Project AKUL/13/19) for financial support for the TEM.

REFERENCES

1. Roger S.A. Fundamentals of green chemistry: efficiency in reaction design. *Chem Soc Rev*. **2012**, 41(4), 1437-1451.

2. Olah G.A. Beyond oil and gas: The methanol economy. *Angew Chem. Int. Ed*. **2005**, 44, 2636-2639**.**

3. Sholl D.S. Seven chemical separations. *Nature*. **2016**, 532, 435-437.

4. Baerlocher, C.; McCusker, L. B. Database of Zeolite Structures. http://www.iza-structure.org/databases/. (August 9, 2022)

5. Dong, G.; Li, H.; Chen, V.; Challenges and opportunities for mixed-matrix membranes for gas separation. *J. Mater. Chem. A.* **2013**, 1 (15), 4610-4630.

6. Pham, T. D.; Lobo, R. F.; Adsorption equilibria of CO2 and small hydrocarbons in AEI-, CHA-, STT-, and RRO-type siliceous zeolites. *Microporous Mesoporous Mater.* **2016**, 236, 100-108.

7. Shu, Y.; Travert, A.; Schiller, R.; Ziebarth, M.; Wormsbecher, R.; Cheng. W. C. Effect of Ionic Radius of Rare Earth on USY Zeolite in Fluid Catalytic Cracking: Fundamentals and Commercial Application. *Top. Catal*. **2015**. 58, 334-342.

8. Vogt, E. T. C.; Weckhuysen, B. M. Fluid catalytic cracking: recent developments on the grand old lady of zeolite catalysis. *Chem. Soc. Rev.* **2015**, 44 (20), 7342-7370.

9. Mao, Y.; Wang, H. F.; Hu, P. Theoretical investigation of NH3-SCR processes over zeolites: A review. *Int. J. Quantum Chem.* **2015,** 115 (10), 618-630.

10. Dusselier, M.; Davis, M. E. Small-Pore Zeolites: Synthesis and Catalysis. *Chem. Rev.* **2018**, 118 (11), 5265-5329.

11. Lv, W.; Wang, S.; Wang, P.; Liu, Y.; Huan, Z.; Li, J.; Dong, M.; Wang, J.; Fan, W. Regulation of Al distributions and Cu^{2+} locations in SSZ-13 zeolites for NH3-SCR of NO by different alkali metal cations. *J. Catal*. **2021**, 393, 190-201.

12. Vennestrøm, P. N. R. ; Janssens, T. V. W. ; Kustov, A.; Grill, M.; Puig-Molina, A.; Lundegaard, L. F.; Tiruvalam, R. R.; Concepción, P.; Corma, A. Influence of lattice stability on hydrothermal deactivation of Cu-ZSM-5 and Cu-IM-5 zeolites for selective catalytic reduction of NOx by NH 3. *J. Catal.* **2014**, 309, 477-490.

13. Guisnet, M.; Gnep, N. S.; Morin, S. Mechanisms of xylene isomerization over acidic solid catalysts. *Microporous Mesoporous Mater*. **2000**, 35-36, 47-59.

14. Irannajad, M.; Kamran, H. H. Removal of Heavy Metals from Polluted Solutions by Zeolitic Adsorbents: a Review. *Environ Process.* **2021**, 8 (1), 7-35.

15. Rangnekar, N.; Mittal, N.; Elyassi, B.; Caro, J.; Tsapatsis, M. Zeolite membranes - a review and comparison with MOFs. *Chem. Soc. Rev.* **2015**, 44 (20), 7128-7154.

16. Cundy, C. S.; Cox, P. A. The hydrothermal synthesis of zeolites: History and development from the earliest days to the present time. *Chem. Rev.* **2003**, 103, 3, 663-702.

17. Ogura, M.; Kawazu, Y.; Takahashi, H.; Okubo, T. Aluminosilicate Species in the Hydrogel Phase Formed during the Aging Process for Crystallization of FAU Zeolite. *Chem.Mater.* **2003**, 15, 2661-2667.

18. Bickel, E. E.; Nimlos, C. T.; Gounder, R. Developing quantitative synthesis-structure-function relations for framework aluminum arrangement effects in zeolite acid catalysis. *J. Catal.* **2021**, 399, 75-85.

19. Di Iorio, J. R.; Li. S.; Jones C. B.; Nimlos, C. T.; Wang, Y.; Kunkes, E.; Vattipalli, V.; Prasad, S.; Moini, A.; Schneider, W. F.; Gounder, R. Cooperative and Competitive Occlusion of Organic and Inorganic Structure Directing Agents within Chabazite Zeolites Influences Their Aluminum Arrangement. *J. Am. Chem. Soc*. **2020**, 142, 10, 4807-4819.

20. Dědeček, J.; Tabor, E.; Sklenak, S. Tuning the Aluminum Distribution in Zeolites to Increase their Performance in Acid-Catalyzed Reactions. *ChemSusChem*, **2019**, 12, 556-576.

21. Le, T. T.; Chawla, A.; Rimer, J. D. Impact of acid site speciation and spatial gradients on zeolite catalysis. *J. Catal*. **2020**, 391, 56-68.

22. Danilina, N.; Krumeich, F.; Castelanelli, S. A.; Van Bokhoven, J. A. Where are the active sites in zeolites Origin of aluminum zoning in ZSM-5. *J. Phys. Chem. C.* **2010**, 114, 14, 6640-6645.

23. Shin, J.; Ahn, N. H.; Cho, S. J.; Ren, L.; Xiao, F. S.; Hong, S. B. Framework Al zoning in zeolite ECR-1. *Chem. Commun*. **2014**, 50, 1956-1958.

24. Verboekend, D.; Nuttens, N.; Locus, R.; Van Aelst, J.; Verlome, P.; Groen, J. C.; Pérez-Ramirez, J.; Sels, B. F. Synthesis, characterisation, and catalytic evaluation of hierarchical faujasite zeolites: Milestones, challenges, and future directions. *Chem. Soc. Rev*. **2016**, 45 (12), 3331-3352.

25. Verboekend, D.; Pérez-Ramírez, J. Desilication mechanism revisited: Highly mesoporous all-silica zeolites enabled through pore-directing agents. *Chem. Eur. J.* **2011**, 17(4), 1137-1147.

26. Ennaert, T.; Van Aelst, J.; Dijkmans, J.; De Clercq, R.; Dusselier, M.; Verboekend, D.; Sels, B. F. Potential and challenges of zeolite chemistry in the catalytic conversion of biomass. *Chem. Soc. Rev.* **2016**, 45, 584-611.

27. Devos, J.; Shah, M. A.; Dusselier, M. On the key role of aluminium and other heteroatoms during interzeolite conversion synthesis. *RSC. Adv.* **2021**, 11(42), 26188-26210.

28. Bermejo-deval, R.; Gounder, R.; Davis, M. E. Framework and Extra framework Tin Sites in Zeolite Beta React Glucose Differently. *ACS. Cat.* **2012,** 2, 12, 2705-2713.

29. Deneyer, A.; Ke, Q.; Devos, J.; Dusselier, M. Zeolite Synthesis under Nonconventional Conditions: Reagents, Reactors, and Modi Operandi. *Chem. Mater*. **2020**, 32 (12), 4884-4919.

30. Bruter, D. V.; Pavlov, V. S.; Ivanova, I. I. Interzeolite Transformations as a Method for Zeolite Catalyst Synthesis. *Pet. Chem*. **2021**, 61 (3), 251-275.

31. Sano, T.; Itakura, M.; Sadakane, M. High Potential of Interzeolite Conversion Method for Zeolite Synthesis. *J. Japan Pet. Inst.* **2013**, 56 (4), 183-197.

32. Mlekodaj, K.; Bernauer, M.; Olszowka, J. E.; Klein, P.; Pashkova, V.; Dědeček, J. Synthesis of the Zeolites from SBU: An SSZ-13 Study. *Chem Mater*. **2021**, 33 (5), 1781-1788.

33. Qin, W.; Jain, R.; Robles Hernández, F. C.; Rimer, J. D. Organic-Free Interzeolite Transformation in the Absence of Common Building Units. *Chem - A Eur J.* **2019,** 25 (23), 5893-5898.

34. Devos, J.; Bols, M. L.; Plessers, D. ; Van Goethem, C.; Seo, J. W.; Hwang, S.-J.; Sels, B. F.; Dusselier, M. Synthesis−Structure−Activity Relations in Fe-CHA for C−H Activation: Control of Al Distribution by Interzeolite Conversion. *Chem. Mater.* **2020**, 32, 273-285.

35. Lee, S.; Nimlos, C. T.; Kipp, E. R.; Wang, Y.; Gao, X.; Schneider, W. F.; Lusardi, M.; Vattipalli, V.; Prasad, S.; Moini, A.; Gounder, R. Evolution of Framework Al Arrangements in CHA Zeolites during Crystallization in the Presence of Organic and Inorganic Structure Directing Agents. *Cryst. Growth Des.* **2022**, 22, 10, 6275-6295.

36. Devos, J.; Robijns, S.; Van Goethem, C.; Khalil, I.; Dusselier, M. Interzeolite Conversion and the Role of Aluminum: Toward Generic Principles of Acid Site Genesis and Distributions in ZSM-5 and SSZ-13. *Chem. Mater.* **2021**, 33 (7), 2516-2531.

37. Muraoka, K.; Sada, Y.; Shimojima, A.; Chaikittisilp, W.; Okubo, T. Tracking the rearrangement of atomic configurations during the conversion of FAU zeolite to CHA zeolite. *Chem. Sci.* **2019,** 10, 8533-8540.

38. Marsden, G.; Kostetskyy, P.; Sekiya, R. S.; Hoffman, A.; Lee, S.; Gounder, R.; Hibbitts, D.; Broadbelt, L. J. Quantifying Effects of Active Site Proximity on Rates of Methanol Dehydration to Dimethyl Ether over Chabazite Zeolites through Microkinetic Modeling. *ACS Mater Au.* **2021**, 2, 2, 163-175.

39. Kester, P. M.; Crum, J. T.; Li, S.; Schneider, W. F.; Gounder, R. Effects of Brønsted acid site proximity in chabazite zeolites on OH infrared spectra and protolytic propane cracking kinetics. *J. Catal*. **2021**, 395, 210-226.

40. Dědeček, J.; Sobalík, Z.; Wichterlová, B. Siting and Distribution of Framework Aluminium Atoms in Silicon-Rich Zeolites and Impact on Catalysis. *Catal. Rev. – Sci. Eng.* **2012,** 54, 135-223.

41. Dědeček, J.; Kaukcy, D.; Wichterlová, B.; Gonsiorova, O. Co^{2+} ions as probes of Al distribution in the framework of zeolites. ZSM-5 study. *Phys. Chem. Chem. Phys.* **2002**, 4 (21), 5406-5413.

42. Nimlos, C. T.; Hoffman, A. J. ; Hur, Y. G. ; Lee, B. J.; Di Iorio, J. R.; Hibbitts, D. D.; Gounder, R. Experimental and Theoretical Assessments of Aluminum Proximity in MFI Zeolites and Its Alteration by Organic and Inorganic Structure-Directing Agents. *Chem. Mater.* **2020**, 32 (21), 9277-9298.

43. Dempsey, E.; Kühl, G. H.; Olson, D. H. Variation of the lattice parameter with aluminum content in synthetic sodium faujasites. Evidence for ordering of the framework ions. *J. Phys. Chem*. **1969**, 73, 2, 387-390.

44. Nishitoba, T.; Yoshida, N.; Kondo, J. N.; Yokoi, T. Control of Al Distribution in the CHA-Type Aluminosilicate Zeolites and Its Impact on the Hydrothermal Stability and Catalytic Properties. *Ind. Eng. Chem. Res.* **2018**, 57, 11, 3914-3922.

45. Di Iorio, J. R.; Gounder, R. Controlling the Isolation and Pairing of Aluminum in Chabazite Zeolites Using Mixtures of Organic and Inorganic Structure-Directing Agents. *Chem. Mater.* **2016**, 28 (7), 2236-2247.

46. Dědeček, J.; Balgová, V.; Pashkova, V.; Klein, P.; Wichterlová, B. Synthesis of ZSM-5 zeolites with defined distribution of Al atoms in the framework and multinuclear MAS NMR analysis of the control of Al distribution. *Chem. Mater.* **2012**, 24 (16), 3231-3239.

47. Pashkova, V.; Klein, P.; Dedecek, J.; Tokarová, V.; Wichterlová, B. Incorporation of Al at ZSM-5 hydrothermal synthesis. Tuning of Al pairs in the framework. *Microporous Mesoporous Mater.* **2015**, 202, 138-146.

48. Kinrade, S. D.; Pole, D. L. Effect of Alkali-Metal Cations on the Chemistry of Aqueous Silicate Solutions. *Inorg. Chem.* **1992**, 31 (22), 4558-4563.

49. Nagy, J. B.; Bodart, P.; Collette, H.; et al. Characterization of crystalline and amorphous phases during the synthesis of (TPA, M)-ZSM-5 zeolites (M = Li, Na, K). *J. Chem. Soc., Faraday Trans. 1,* **1989**, 85 (9), 2749-2769.

50. Aiello, R.; Crea, F.; Nastro, A.; Subotic, B.; Testa, F. Influence of cations on the physicochemical and structural properties of aluminosilicate gel precursors. I. chemical and thermal properties. *Zeolites*. **1991**, 11, 767-775.

51. Wijnen, P. W. J. G.; Beelen, T. P. M.; De Haan, J. W.; Van De Ven, L. J. M.; Van Santen, R. A. The structure directing effect of cations in aqueous silicate solutions. A 29Si-NMR study. *Colloids and Surfaces*. **1990**, 45, 255-268.

52. McCormick, A. V.; Bell, A. T.; Radke, C. J.. Effect of alkali metal cations on silicate structures in aqueous solution. *ACS Symp. Ser*. **1988**, 368, 222-235.

53. Asselman, K.; Pellens, N.; Radhakrishnan, S.; Chandran, V. C.; Martens, J. A.; Taulelle, F. Verstraelen, T. Hellström, M.; Breynaert, E.; Kirschhock, C. E. A. Super-ions of sodium cations with hydrated hydroxide anions: Inorganic structure-directing agents in zeolite synthesis. *Mater. Horiz.* **2021**, 8 (9), 2576-2583.

54. Vattipalli, V.; Paracha, A. M.; Hu, W.; Chen, H.; Fan, W. Broadening the Scope for Fluoride-Free Synthesis of Siliceous Zeolites. *Angew. Chemie – Int. Ed.* **2018,** 57 (14), 3607-3611.

55. Lodesani, F.; Menziani, M. C.; Maeda, K.; Takato, Y.; Urata, S.; Pedone, A. Disclosing crystal nucleation mechanism in lithium disilicate glass through molecular dynamics simulations and free-energy calculations. *Sci. Rep.* **2020**, 10 (1), 1-14.

56. Bernard, E.; Yan, Y.; Lothenbach, B. Effective cation exchange capacity of calcium silicate hydrates (C-S-H). *Cem. Concr. Res*. **2021**, 143, 106393.

57. Ivanova, I. I.; Aiello, R.; Nagy, J. B.; Crea, F.; Derouane, E. G; Dumont, N.; Nastro, N.; Subotic, B.; Testa, F. Influence of cations on the physicochemical and structural properties of aluminosilicate gel precursors. II. Multinuclear magnetic resonance characterization. *Microporous Mater*. **1994**, 3 (3), 245-257.

58. Muraoka, K.; Chaikittisilp, W.; Okubo, T. Energy Analysis of Aluminosilicate Zeolites with Comprehensive Ranges of Framework Topologies, Chemical Compositions, and Aluminum Distributions. *J. Am. Chem. Soc.* **2016**, 138, 19, 6184-6193.

59. Thomas, A. M.; Nag, S.; Yadav, D. K.; Uniyal, S.; Uma, S.; Subramanian, Y. A new empirical potential for zeolite with variable Si/Al ratio: Simulations vs. experiments. *Microporous Mesoporous Mater.* **2020**, 300, 110119.

60. Eilertsen, E. A.; Nilsen, M. H.; Wendelbo, R.; Olsbye, U.; Lillerud, K. P. Synthesis of High Silica CHA Zeolites with Controlled Si/Al Ratio. *Stud. Surf. Sci. Catal.* **2008**, 174, 265-268.

61. Kumar, M.; Luo, H.; Román-Leshkov, Y.; Rimer, J. D. SSZ-13 crystallization by particle attachment and deterministic pathways to crystal size control. *J. Am. Chem. Soc*. **2015**, 137,40,13007-13017.

62. Chawla, A.; Linares, N.; Li, R.; García-Martínez, J.; Rimer, J. D. Tracking Zeolite Crystallization by Elemental Mapping. *Chem. Mater.* **2020**, 32 (7), 3278-3287.

63. Iwame, M.; Suzuki, Y.; Plévert, J.; Itabashi, K.; Ogura, M.; Okubo, T. Location of Alkali Ions and their Relevance to the Crystallization of Low Silica X Zeolite. *Cryst. Growth Des.* **2010,** 10, 8, 3471-3479.

64. Ahn, S. H.; Lee, H.; Hong, S. B. Crystallization Mechanism of Cage-Based, Small-Pore Molecular Sieves: A Case Study of CHA and LEV Structures. *Chem. Mater.* **2017**, 29, 13, 5583-5590.

65. Zones, S. I. ; Lew, C. M . ; Xie, D. ; Davis, T. M. ; Schmidt , J. E.; Saxton, R. J. Studies on the use of faujasite as a reagent to deliver silica and alumina in building new zeolite structures with organo-cations. *Microporous Mesoporous Mater.* **2020**, 300, 110162.

TOC Graphic:

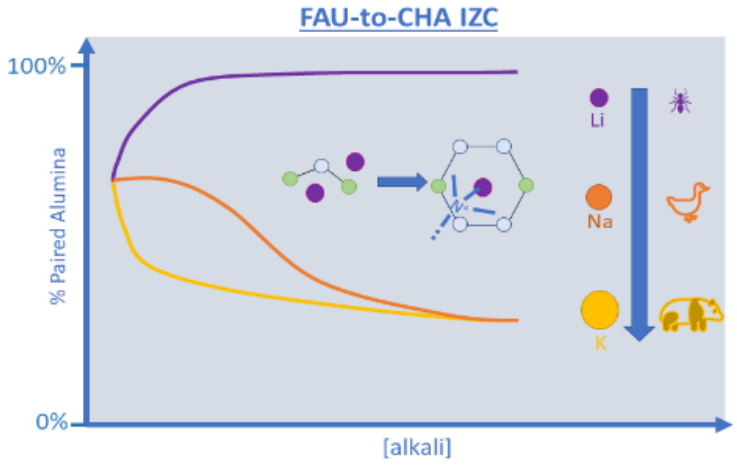

The effect of alkali cations (Li,Na and K) on the aluminum distribution and crystallization kinetics of an Inter Zeolite Conversion (IZC) from FAU-to-CHA was investigated, revealing the positive effect Li-cations exert on both of these. In this way, by addition of Li^+ during synthesis, the first 'fully paired' SSZ-13 zeolite was obtained.